LITHOS 438–439 (2023) 107015

Contents lists available at ScienceDirect

LITHOS

journal homepage: www.elsevier.com/locate/lithos

New insights on the porosity and grain features of Al Haggounia 001, an impact-melt meteorite

Paola Manzari [a], Daniela Mele [b], Gioacchino Tempesta [b], Giovanna Agrosì [b,*]

[a] Italian Space Agency, Rome, Italy
[b] Department of Earth and Geo-environmental, University of Bari "Aldo Moro", Bari, Italy

ARTICLE INFO

Keywords:
EL3 impact melt meteorite 1
Pores and vesicles 2
Sulfides 3

ABSTRACT

In the frame of a broader study on impact effects on meteorites microstructures and mineralogy, we studied the internal structures and grain features of Al Haggounia 001 meteorite, a very interesting EL3 impact melt characterized by a strong porosity. The study was carried out using a 3D reconstruction obtained by micro-Computed x-ray Tomography (μ-CT) supported by chemo-mineralogical characterization obtained by SEM-EDS. The fragments examined consist of a matrix of enstatite, plagioclase, with minor phases such as sulfides, oxides, and phosphides. Only one relict chondrule was observed that consists of a radial pyroxene with enstatite composition, Na plagioclase and silica mesostasis. SEM-EDS analyses reveal that the average composition of pyroxene and plagioclase is ($En_{98.4}$ Fs_0 $Wo_{1.6}$) and (Ab_{80} An_{12} Or_8), respectively. The minor phases found are daubréelite, schreibersite, oldhamite, troilite, graphite, tiny kamacite grains survived to the weathering, and N-bearing oxide. In addition to primary phases, terrestrial products as jarosite and halite were found. Kamacite appears variably oxidized. HR-SEM images reveal resorption features as well as rounded etch pits on the surfaces of daubréelite, holes on plagioclase and scalloped enstatite crystals. The μ-CT measurements show an uneven porosity with an average percentage of about 15% that consists averagely of open pores (12%) and closed pores (3%) with irregular to round shapes. The methodological approach based on volumetric investigation provides information about the spatial distribution, volume percentage and shape of voids and mineralogical phases with different density and adds new elements about the origin of porosity in this meteorite.

1. Introduction

The "fossil meteorite" [1 (Bunch et al., 2014)], Al Haggounia 001, is a EL3 impact melt rock (Rubin, 2016). It is an interesting meteorite because, with paired samples named Northwest Africa (NWA), with a total mass of about 3 tons (MBD), represent the largest enstatite meteorite known. This meteorite was found in 2006 in western Sahara in sedimentary rocks such as conglomerates. Due to lack of expected metal and well-defined chondrules, low abundances of sulfides, and the presence of vesicles, Al Haggounia 001 suffered a complex classification history. In a first moment was classified as an aubrite; whereas its paired fragments (e.g., NWA 002, 1067, 2736, 2828, 2965, 7401) were classified not only as aubrites but also as different types of enstatite chondrites (EL6, EL6/7, E6, EL3) (e.g., Irving et al., 2010; Kuehner et al., 2006; Lowe et al., 2005). Recently, Rubin (2015, 2016) reclassified this meteorite as "vesicular, incompletely melted, EL chondrite impact melt rock[s]."

As an EL3 impact melt, this meteorite belongs to enstatite meteorite clan that, among the other groups of meteorites, show to have a highly reduced nature and mineralogy with fO_2 similar to that of Mercury estimated using data from the MErcury Surface, Space ENvironment, GEochemistry, and Ranging (MESSENGER) spacecraft (McCubbin, 2017; McCubbin et al., 2012; Udry et al., 2019; Zolotov et al., 2013). Al Haggounia 001 is characterized by the presence of graphite and sulfides (oldhamite, alabandite and troilite) that represent typical phases found in reduced enstatite chondrite (Rubin, 2016; Szurgot et al., 2011). This meteorite exhibits a terrestrial age of about 23,000 ±2000 yr., as measured by ^{14}C dating (Chennaoui-Aoudjehane et al., 2007) and shows, also, a heavily weathering (W4–W5 grade).

An unusually high porosity characterizes Al Haggounia 001 (Kuehner et al., 2006). This singular feature was previously studied by Rubin (2016) that observed voids on thin sections of Al Haggounia 001 and its paired meteorite fragments; some were rounded, some irregular and other showed elongated shape. The apparent diameter measured on 40

* Corresponding author.
E-mail address: giovanna.agrosi@uniba.it (G. Agrosì).

https://doi.org/10.1016/j.lithos.2022.107015
Received 13 August 2022; Received in revised form 16 December 2022; Accepted 28 December 2022
Available online 31 December 2022

Fig. 1. Optical image of the of Al Haggounia 001 meteorite fragment. The red rectangles, named B1 and B2, represent the volumes analyzed by micro-X-ray-Computed Tomography (μ-CT). (For interpretation of the references to colour in this figure legend, the reader is referred to the web version of this article.)

voids ranged between 50 and 610 μm with an average of around 200 ± 140 μm (Rubin, 2016). The modal abundance of voids observed by optical observations in transmitted light of NWA 7401 is 6.8 vol% (Rubin, 2016). The same author also found petrographic features consistent with incompletely melted rocks by impact. In fact, he observed vesicles on NWA 7401, paired with Al Haggounia 001, similar to those observed on ordinary-chondrite impact-melt breccias and impact-melt rocks.

The finding of porosity in meteorites and its origin was a long time debated. The first studies were done by Alexayeve (1958), Stacy et al. (1961) and Keil (1962). More recently, Consolmagno et al. (2008) compared meteorite density and porosity and physical properties of their parent bodies and they focused on chondrites belonging to different classes and petrological group. Soini et al. (2020), studied the thermal conductivity, the thermal diffusivity and porosity mainly on the chondrite groups. In the last years, the origin of porosity was investigated directly visualizing the volume distribution, density, and shape of pores by means of a useful and innovative technique: micro–X-ray Computed Tomography (μ-CT). This non-destructive technique has been increasingly used in the meteoritics studies to explore phase distribution, microstructures, crystal habits or grains, occurrences of porosity, melt veins and fractures in a 3D reconstruction of a small meteorite volume, as reported in reviews by Pratesi et al. (2014) and Hanna and Ketcham, (2018). This technique has been mainly applied to the study of texture and distribution of mineral phases, shapes of chondrules and pore distribution on chondrites (Kalasová et al., 2020; Panerai et al., 2021 and references therein); on meteorites of Mars (Nascimento-Dias et al., 2019; Porfido et al., 2020); on enstatite meteorites, (Krzesińska et al., 2019); on stardust impact tracks (Tsuchiyama et al., 2009), on silicate inclusions in meteoritic chromite grains (Alwmark et al., 2011), on splash-form moldavites (Pratesi et al., 2014), on micrometeorites (Dionnet et al., 2020) and on carbonaceous chondrites (Hanna et al., 2022; Zhang et al., 2021).

In the present study, μ-CT analyses were performed, for the first time, to study the porosity and grain features of Al Haggounia 001 meteorite. In particular, we combined micro-CT data with chemo-mineralogical data acquired by Scanning Electron Microscopy (SEM) to reconstruct the 3D internal structure of this meteorite. This methodological approach allowed to obtain information about total porosity, to distinguish between open and closed pores, to measure the respective vol% and sizes; to perform observations on grain features; to determine the relationships among spatial distribution of pores and the different mineralogical phases. The results obtained permit to add new elements on the origin of porosity and its implications on the evolution history of this very singular meteorite.

2. Materials and methods

We studied one standard rectangular thin section and a slab section (width = 17 mm; depth = 2.9 mm; height = 6.2 mm) taken from the same fragment of Al Haggounia 001. Modal abundances of phases were determined on the thin section by optical observations. The thin section and the slab were investigated by Scanning Electron Microscopy (SEM), after graphite and gold-coating, respectively. Even if the carbon coating is better for analyses, the gold coating was also done to better identify the C-rich phases. To improve the information, the surface of slab investigated by SEM is not adjacent to the region where thin section was cut.

Table 1
μ-CT scanning parameters.

μX-CT scanner parameters		Reconstruction parameters	
Pixel Size (μm)	3	Smoothing	4
X-ray Voltage (Kv)	85	Ring Artifact Correction	7
X-ray Current (μA)	118	Beam Hardening Correction (%)	46
Rotation Step (degrees)	0.28	–	
Filter	Al 0.5 mm	–	
Frame Averaging	5	–	

The slab sample was analyzed also by micro–X-ray Computed Tomography (μ-CT). For convenience, the μ-CT acquisition, was performed on two regions of slab, named B1 and B2 (Fig. 1).

The SEM microscope used is Zeiss LEO, model EVO-50XVP, housed at the Department of Earth and Geo-environmental Sciences, University of Bari Aldo Moro, coupled with an X-max (80 mm2) energy dispersive (ED) Silicon drift Oxford detector (Oxford Instruments) equipped with a Super Atmosphere Thin Window ©. It has secondary (SE) and back-scattered electron (BSE) detectors. Microanalysis was performed with the Silicon drift ED detector using operating conditions of 15 kV accelerating potential, 500 pA probe current, 5 nm beam size, about 25,000 output counts per second (cps) as average count rate on the whole spectrum, counting time of 50 s and 8.5 mm working distance. X-ray intensities were converted to wt% (*w*/w) oxides by XPP correction scheme developed by Pouchou and Pichoir (1991), granted as quantitative software support by Oxford-Link Analytical (UK). Given the composition of the analyzed mineral phases, the 1σ precision corresponded to the following values: SiO2 = 0.10–0.20 wt%, TiO2 = 0.08–0.10 wt%, Al2O3 = 0.08–0.13 wt%, FeO = 0.05–0.15 wt%, MnO = 0.04–0.6 wt%, MgO = 0.08–0.13 wt%, CaO = 0.04–0.14 wt%, Na2O = 0.04–0.06 wt% and K2O = 0.04–0.12 wt%. The accuracy of the analytical data was also checked using several standard minerals manufactured by Micro-Analysis Consultants Ltd. (UK).

Analyses by μ-CT were performed with Bruker Skyscan 1172 high-resolution μX-CT scanner, at the Department of Chemistry, University of Bari Aldo Moro. The instrument operates at an X-ray Voltage of 100

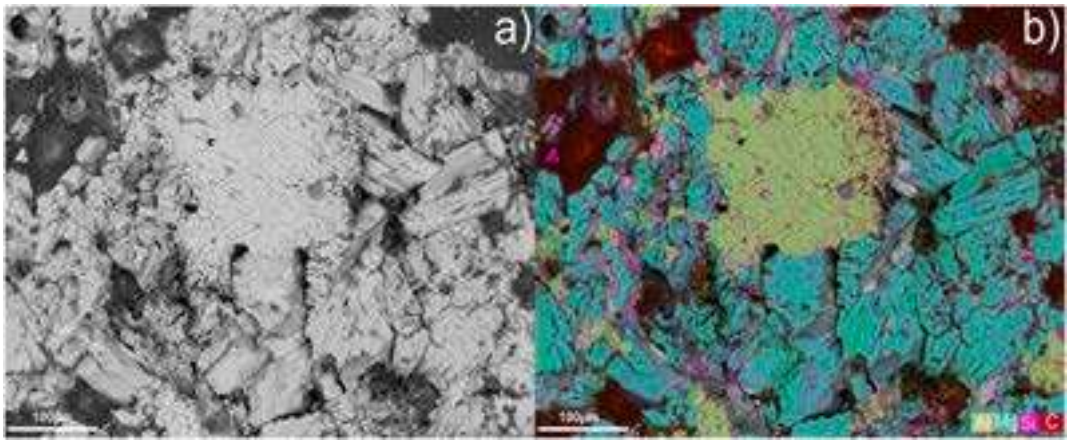

Fig. 2. a) SEM-BSE image of Al Haggounia 001 thin section. b) Elemental maps overlayed on BSD image. Blue = enstatite; yellow = plagioclase. (For interpretation of the references to colour in this figure legend, the reader is referred to the web version of this article.)

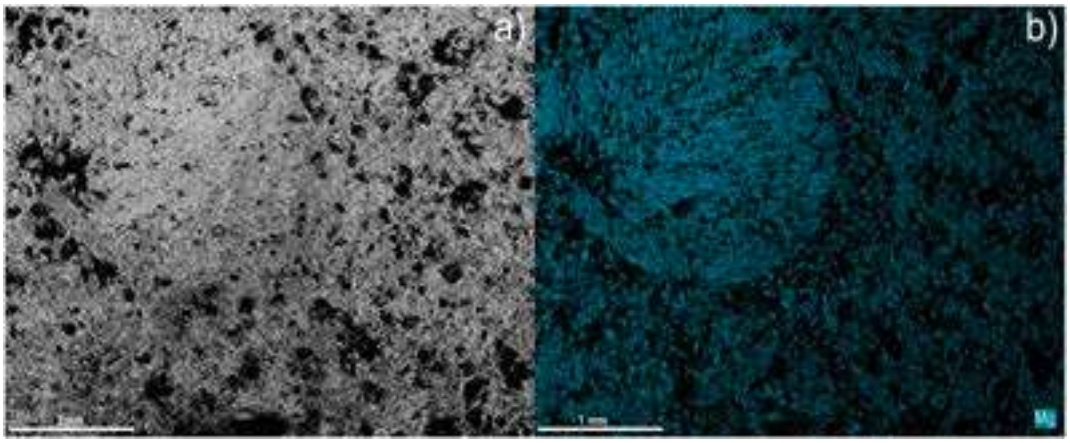

Fig. 3. Radial pyroxene chondrule in the Al Haggounia 001 slab a) SEM-BSE image; b) Mg elemental map.

kV using an Al filter of 0.5 mm (see scanning and reconstruction parameters in Table 1). Bruker's NRecon software was used to reconstruct μX-CT projection images into two-dimensional cross section (slices) by applying the Feldkamp algorithm (Feldkamp et al., 1984). Cross-section parameters are shown in Table 1. The CTAnalyser (version 1.20.8.0, Bruker μ-CT) and CTvox (version 3.3.0 r1403, Bruker μ-CT) software were used for measuring quantitative parameters and for the 3D rendering, respectively. To ensure a data reproducibility and a proper comparison between different studies on porosity (Jaques et al., 2021), additional information was reported in the supplementary material with a detailed description of the segmentation procedure by "Step by step" image processing workflow for 3D data.

3. Results

3.1. Scanning electron microscope analyses

The chemical and mineralogical analyses were carried out on the slab and on thin section of the fragment of Al Haggounia 001, acquiring chemical maps and performing in-situ compositional. The results show that the sample consists of a matrix of about 62% of enstatite and 36% of plagioclase (Fig. 2) with minor phases (2%) that can be divided in primary and secondary phases. Primary minor phases found are sulfides (daubréelite, oldhamite and troilite), phosphides (scheirbersite), graphite, and N-bearing phase (sinoite) and tiny kamacite grains (2–5 μm in diameter) survived to the weathering. Secondary minerals grown in terrestrial environment (Rubin, 2016) exhibit a composition of jarosite and halite (1.5%), whereas some kamacite grains exhibit variable degree of oxidation.

Only one relict chondrule was observed on the surface of the slab section (Fig. 3). The chondrule consists of a radial pyroxene with

Table 2
SEM-EDS microanalyses (wt%). Average composition of silicates (10-point analyses for each phase).

Plagioclase							
Oxides	Na_2O	MgO	Al_2O_3	SiO_2	K_2O	CaO	TOT
Wt%	**9.27 ± 0.05**	**2.00 ± 0.03**	**19.14 ± 0.07**	**65.14 ± 0.13**	**1.46 ± 0.03**	**2.39 ± 0.04**	**99.42**
cnd-member fractions (mol %)	$Ab_{80.23}An_{11.45}Or_{8.32}$						
Enstatite oxides	**MgO**	**Al_2O_3**	**SiO_2**	**CaO**		**TOT**	
Wt%	**39.15 ± 0.08**	**0.56 ± 0.03**	**59.26 ± 0.12**	**0.88 ± 0.03**		**99.85**	
Calculated end-member fractions (mol %)	$En_{98.4}Fs_0Wo_{1.6}$						

Table 3
SEM-EDS microanalyses (wt%). Average composition of minor phases (5-point analyses for each phase).

Jarosite							
Elements	**O**	**P**	**Cl**	**K**	**Ti**	**Cr**	**Fe**
Wt%	**39.50 ± 0.16**	**12.95 ± 0.08**	**0.33 ± 0.03**	**7.48 ± 0.07**	**0.52 ± 0.05**	**0.90 ± 0.07**	**38.32 ± 0.18**
Troilite							
Elements	**S**	**Ca**	**Ti**	**Cr**	**Fe**		
Wt%	**37.6 ± 0.09**	**0.09 ± 0.02**	**0.55 ± 0.03**	**0.96 ± 0.04**	**60.79 ± 0.1**		
Daubreelite							
Elements	**S**	**Cr**	**Mn**	**Fe**			
Wt%	**43.89 ± 0.34**	**37.85 ± 0.36**	**2.05 ± 0.27**	**16.21 ± 0.34**			
Schreibersite							
Elements	**P**	**Fe**	**Ni**				
Wt%	**14.42 ± 0.09**	**69.13 ± 0.18**	**16.46 ± 0.18**				
Kamacite							
Elements	**P**	**Fe**	**Ni**				
Wt%	**0.07 ± 0.01**	**96.92 ± 0.13**	**3.01 ± 0.12**				
Sinoite							
Elements	**N**	**O**	**Si**				
Wt%	**20.43 ± 0.19**	**21.44 ± 0.16**	**57.93 ± 0.19**				

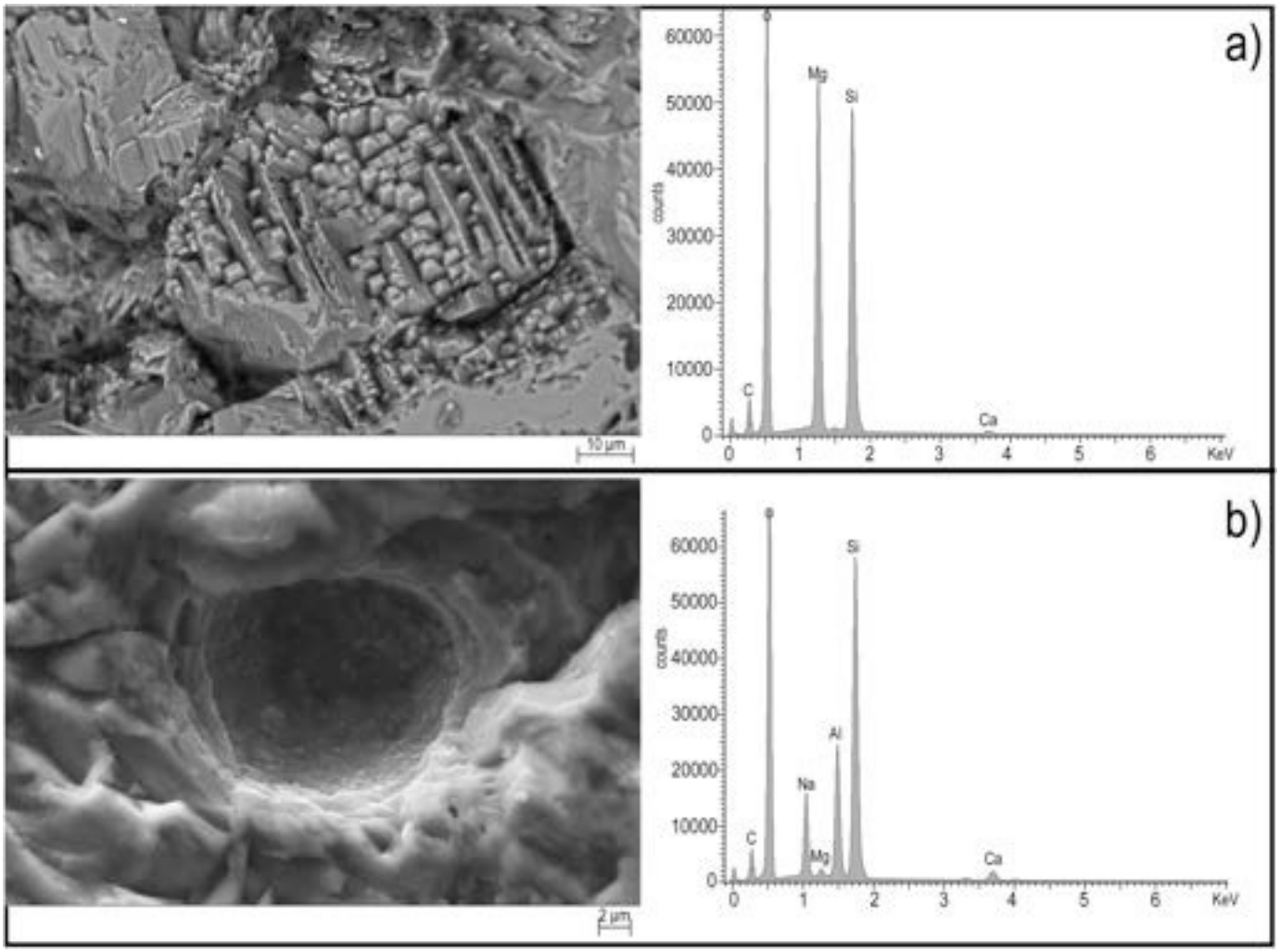

Fig. 4. Images of resorption features on thin section of Al Haggounia 001 a) SEM-BSE image of scalloped enstatite and corresponding EDS spectrum; b) SEM-SE images of sub-spherical and rounded holes on Na-plagioclase and corresponding EDS spectrum.

enstatite composition, Na plagioclase and silica mesostasis, as revealed by optical observation and chemical composition.

SEM-EDS microanalyses show that the average composition of the silicates is $Ab_{80.23}An_{11.45}Or_{8.32}$ for plagioclase and $En_{98.4}Fs_{0}Wo_{1.6}$ for enstatite (Table 2). The compositions of the minor phases are shown in the Table 3.

From the textural point of view, the slab is porous and exhibit resorption features. Voids observed can be distinguished in irregular and rounded shapes. In general, irregular shapes characterize the voids between different crystals.

The resorption features observed regard mainly silicates and Cr-rich sulfides. Enstatite grains often appear as scalloped crystals (Fig. 4a).

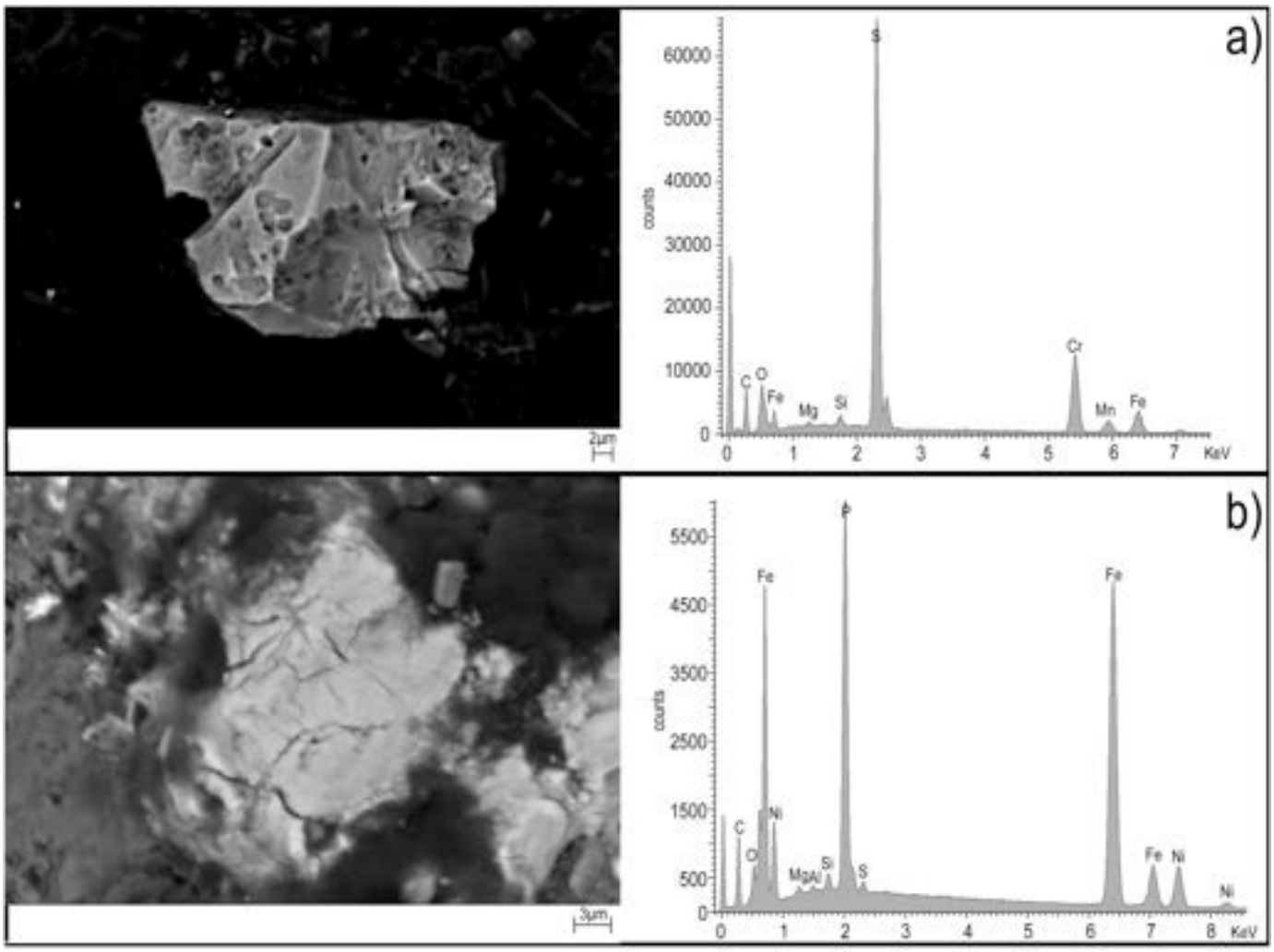

Fig. 5. SEM images and corresponding EDS spectra on thin section of Al Haggounia 001. a) SEM-BSE image of daubréelite grain showing round circular etch pits b) SEM-BSE image of fractured schreibersite grain.

Locally the surface of some plagioclase crystals exhibits rounded holes characterized by smooth walls (Fig. 4b). Grains of daubréelite composition exhibit rounded etch-piths like popped bubbles (Fig. 5a), whereas schreibersite grains show smooth, sometimes fractured surfaces (Fig. 5b).

3.2. *μ-Xray computed tomography (μ-CT)*

The B1 and B2 volumes of the slab of Al Haggounia 001 were investigated by μ-CT (Fig. 6). The images acquired are characterized by different grayscale intensities proportional to the different X-rays absorption of the volume investigated (Agrosì et al., 2019). The not uniformly X-ray absorption is due to the presence of minerals with different X-ray attenuation coefficients and an uneven distribution of voids. In Fig. 6, the phases with highest attenuation coefficient appear white, whereas phases with low to middle attenuation coefficient appear light to medium and dark grey. The attenuation coefficient corresponding to voids is near zero; consequently, the voids appear black.

The micro-CT images reveal that region B1 is quite homogeneous, while region B2 shows different features in the inner and outer part (Fig. 6a). The cross-section images, taken along the B1 and B2 regions, show a variable distribution of phases, an uneven distribution of porosity, and a strong correlation of the spatial distribution of pores (black) with high-density phases (white) (Fig. 6b).

Specifically, the high-density phases (white) are mainly confined near the pores and, in some cases, fill them (Fig. 6). Furthermore, the high-density phases appear most abundant in the outer part of B2 volume. The 3D analysis also allows distinguishing between open and closed pores. Open pores are empty spaces within the meteorite volume that show any connection in 3D to the space outside the object. Closed pores consist of empty spaces in the meteorite volume that are surrounded by solid phases.

To quantify the main components that characterize Al Haggounia 001 slab, five categories were considered selecting thresholds based on peak analyses of the grayscale histogram (0–255) of the rendered volumes.

These categories were assigned as follows: white: range 181–255 of histogram assigned to highest density phases; light grey: range 131–180 assigned to the moderately dense phases; medium grey: 100–130 assigned to moderately less dense phases; dark grey: 30–99 assigned to the less dense phases in the slab. Values of histogram <30 were assigned to pores and materials trapped in them, such as air and low-density epoxy resin used for rock embedding.

The 3D results found on the B1 and B2 volumes show significant differences (Tables 4 and 5).

The total porosity of volume B1 results higher than that of volume B2, significantly decreasing in the upper part of B2, where the maximum percentage of closed pores was observed. The average size of open pores is about 0.42 mm both for B1 and B2 volumes; whereas the average size of closed pores is higher in the B2 outer volume (0.035 mm) than that of

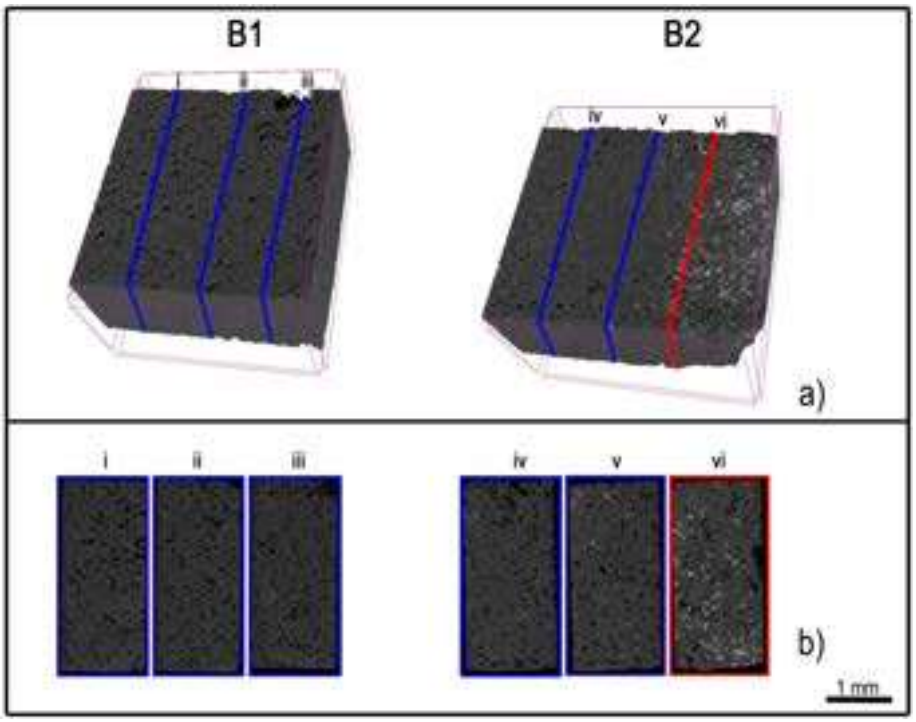

Fig. 6. μ-CT images of Al Haggounia 001 slab. Black = pores. Grey to white = phases with increasing X-ray attenuation coefficient. a) Volume rendering images of B1 and B2 regions. Red line divides the outer part (right) from the inner part (left) of B2 volume. b) cross-section images taken along the blue and red lines of B1 and B2 volumes. (For interpretation of the references to colour in this figure legend, the reader is referred to the web version of this article.)

Table 4
Volume percentage and sizes of pores measured on volumes B1 and B2 and the outer and inner parts of B2.

	Thresholds on greyscale histogram	B1	B2	B2inner	B2outer
Total porosity (vol%)	≤30	17.52	13.08	14.31	9.27
Open pores (vol %)	≤30	15.00	9.47	11.51	5.13
Closed pores (vol %)	≤30	2.52	3.61	2.80	4.14
Solid phases (vol %)	31–255	82.48	86.92	85.69	90.73
Average size of open pores (mm)	≤30	0.041	0.043	0.043	0.041
Average size of closed pores (mm)	≤30	0.024	0.030	0.026	0.035

Table 5
Volume percentage of the main threshold ranges, calculated considering only the solid phases, measured on volumes B1 and B2 and the outer and inner parts of B2.

Grey level	Thresholds on greyscale histogram	B1	B2	B2 inner	B2 outer
White (%)	181–255	0.02	0.06	0.02	0.15
light grey (%)	131–180	0.05	0.52	0.05	1.55
medium grey (%)	100–130	0.09	0.80	0.10	2.36
dark grey (%)	31–99	99.83	98.60	99.82	95.97

closed pores in the B1 and B2 inner volume (0.025 mm) (Table 4 and Fig. 7).

Table 5 reports the percentage of the other four solid categories (181–255, 131–180, 100–130 and 30–99 ranges of histogram values). Their percentages were calculated considering only the volume of solid phases, excluding the porosity volume. The volume percentage of phases with high-density (histogram values between 100 and 255) is significantly higher in the outer part of the B2 volume (about 4%) than B1 volume and the inner part of volume B2 (about 0.170%), confirming what observed qualitatively in Fig. 6a.

3.3. Merging of SEM-EDS and μ-CT data

To quantify approximately the spatial distribution and the volume percentage of mineralogical phases, we merge SEM-EDS microanalyses with the results of the volume rendering segmentation of μ-CT data. The threshold ranges on grey scale histogram were assigned to the corresponding minerals considering the Linear Attenuation Coefficient (LAC) values of the main phases identified with SEM-EDS analyses. LAC was also calculated for iron oxide and hydroxides formed by the oxidation of kamacite, in agreement with the finding of previous studies on Al-Haggounia 001 (Rubin, 2016). Minerals with similar LAC were grouped, and for each group the correspondence with the grayscale colour of thresholding is listed in Table 6.

The data comparison shows that the dark grey phases (33–99 thresholding) consist mainly of silicates (enstatite and plagioclase) with other less abundant phases such as sinoite, graphite and secondary halite. Sulfides and secondary phases such as jarosite, iron oxides and hydroxides represent the intermediate grey scale up to white corresponding to schreibersite and kamacite. The inhomogeneous spatial distribution of phases and pores in the B1 and B2 volumes of slab, their volume percentages, and the different pores sizes are shown in Table 7 and Fig. 7.

The volume percentage of silicates is very high and represents on average 84.00% of the total volume. The moderately and moderately

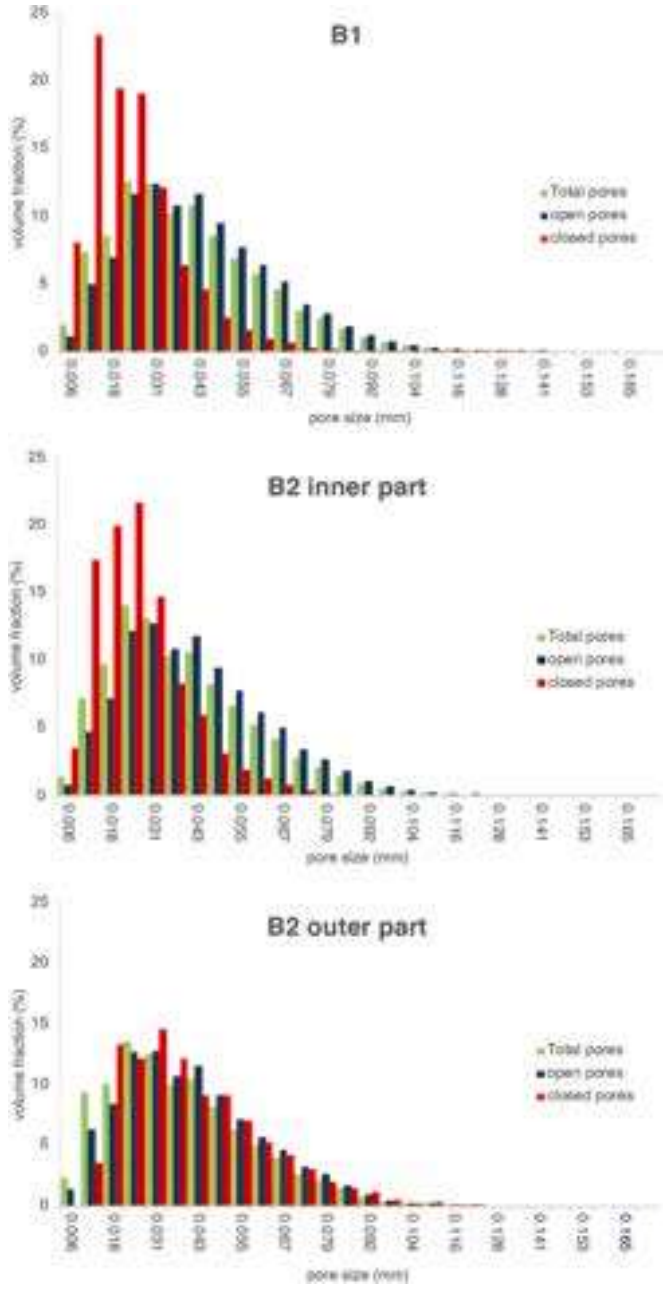

Fig. 7. Pore size distribution histograms of the B1 region and inner and outer parts of the B2 region.

less dense phases, consisting of iron oxides and hydroxides, troilite, daubréelite, jarosite and oldhamite, represent low amounts with significant difference between B1 and B2 region and the outer part of B2 region. Nevertheless, the amount of schreibersite and kamacite could be slightly underestimated because of the spatial resolution of 3 μm used in the μ-CT acquisition (Table 1). Grains smaller than 3 μm could be present, but not considered in this calculation.

4. Discussion

The obtained results show that the studied fragment of Al-Haggounia 001 meteorite is not homogeneous regarding the spatial distribution of porosity and high-density phases. The porosity has been measured on a volume of sample (B1 volume = 1.12×10^{2} mm3; volume of B2 = 1.34×10^{2} mm3), distinguishing, for the first time for this meteorite, between open and closed pores. The average total porosity is almost consistent with a previous volumetric study performed by El Abassi et al. (2013) who found in Al Haggounia 001 meteorite a porosity of 12.4 ± 1.2%, using ultrasonic reflectivity method with a spatial resolution of 0.7 μm and considering only open pores. The average porosity calculated on B1 and B2 is about 12.20% of volume, considering only the open pores. Since the heterogenous texture of Al Haggounia 001 and its paired samples and the different principles of the used techniques with a slightly different spatial resolution, the volume percentage of open pores, in both cases measured on a volume of meteorite, fit very well. Nevertheless, in our case, the finding of closed pores significantly increases locally the value of total porosity. The porosity in rocks is generally related to weathering processes through a combination of volumetric strain and chemical mass loss (Hayes et al., 2019). However, the origin of porosity in meteorites is a still debated topic. The correlation between terrestrial weathering and porosity of chondrites has been matter of study in several scientific paper based on estimation of number of pores by modal analyses on bidimensional objects, such as thin section of SEM-BSE images, or by volumetric methods (e.g., pycnometer) able to determine only interconnected holes. In literature, these data have been often correlated to iron-oxidation state, obtained by Mössbauer spectroscopy, to determine the relationships between porosity and degree of weathering (Bland et al., 2006; Consolmagno et al., 2008; Irving et al., 2010; Li et al., 2019). In particular, Bland et al. (2006) and Consolmagno et al. (2008) hypothesized that meteorites weathering occurs in a two-stage process: a rapid partial oxidation (the time of this stage depend on the climate where it fell) followed by a much slower destruction of the meteorite fabric (up to thousands of years for dry desert meteorites). They hypothesized a correlation between weathering rate and initial porosity of the sample. Irving et al. (2010) ascribed porosity to a differential dissolution of the primary metal in a semi-arid environment. Li et al. (2019), comparing results obtained on falls and find meteorites, found high porosity (up to 17–18%) in fall ordinary chondrites with a very low or absent weathering (W0-W1) and a significantly reduced porosity (up to 12%) in find chondrites. They ascribed a reduction of porosity to a space filling by terrestrial weathering products. Most recently, with the increasing use of μ-CT, the studies on meteorite porosity took advantage from this non-destructive, non-contaminating, and high precision method, able to detect also closed pores. The finding of closed pores further complicates the attempt to explain the origin of porosity in meteorites. Kalasová et al. (2020) studying a recovered ordinary chondrite with a shock stage S2 and a weathering grade (W0-W1), assigned closed pores to natural porosity and cracks to weathering influence. Hanna et al. (2022) found in carbonaceous chondrites sub-micrometric closed pores in chondrule olivine and hypothesized a primary origin associated with chondrule crystallization in the nebula, most likely due to vapor or shrinkage bubbles associated with melt inclusions.

The origin of porosity found in this study on Al Haggounia 001 can be explained also considering the grain features, the mineralogical composition and relationships between voids and solid phases of this meteorite. The studied fragment shows a very low content of solid phases, excluding the silicates. The phases corresponding to 100–255 of thresholding in the 3D volume rendering, show a volume percentage of 0.088% in region B1, 0.146% in the inner part of volume B2 and a higher value of 3.696% in the outer part of volume B2. If we consider that the increase of high-density phases in the outer part of B2 is due to a high quantity of secondary phases (jarosite and iron oxides and hydroxides), sulfides, kamacite and schreibersite represent a very little amount. Furthermore, among the sulfides found in this study, troilite represents a very tiny amount. This finding contrasts with the composition of EL3 chondrites that generally contain about 10 vol% of sulfides with a prevalent presence of troilite (about 90 vol%) (El Goresy et al., 2017; Weisberg and Kimura, 2012). Grains smaller than 3 μm could not be found because of the spatial resolution of μ-CT analyses, but this resolution-limit is insufficient to explain such a little number of sulfides. The low content of these phases could be ascribed not only to the severe

Table 6
Minerals with similar LAC grouping under same grayscale colour. LAC calculated by MuCalc software (Hanna and Ketcham, 2017) and MXLAC software (Bam et al., 2020).

Mineralogical phases	Formula	LAC (Energy =60 keV)	Colour categories	Thresholds on grayscale histogram
kamacite	(Fe,Ni)	9.444	white	181–255
schreibersite	$(Fe,Ni)_3P$	7.750		
wustite	$Fe^{2+}O$	5.4		
hematite	$Fe^{3+}_2O_3$	4.729	light grey	131–180
troilite	$Fe^{2+}S$	4.210		
goethite	$Fe^{3+}O(OH)$	3.57		
daubreelite	$Fe^{2+}Cr_2S$	2.880		
jarosite	$KFe^{3+}_3(SO_4)_2(OH)_6$	1.760	medium grey	100–130
oldhamite	$Ca_{0.9}Mg_{0.05}Fe^{2-}_{0.05}S$	1.370		
enstatite	$Mg_2Si_2O_6$	0.871		
halite	NaCl	0.771		
sinoite	Si_2N_2O	0.740	dark grey	31–99
silica mesostasis	SiO_2	0.666		
Na-plagioclase	$Na_{0.95}Ca_{0.05}Al_{1.05}Si_{2.95}O_8$	0.642		
graphite	C	0.390		

Table 7
volume percentage of the five categories of thresholds based on peak analyses of the grayscale histogram (0–255) of the whole rendered volumes.

Phases	Thresholding	Vol% B1	Vol%B2 inner	Vol% B2 outer
kamacite				
schreibersite	181–255	0.01	0.02	0.14
wustite				
hematite				
troilite				
goethite	131–180	0.03	0.044	1.41
daubreelite				
jarosite				
oldhamite	100–130	0.05	0.085	2.15
enstatite				
halite				
sinoite				
Silica mesostasis				
albite				
graphite	31–99	82.39	85.54	87.03
Total porosity	≤ 30	17.52	14.31	9.27
Closed pores		2.52	3.17	4.14

weathering that caused a progressive oxidation and dissolution of primary phases. Nevertheless, the weathering could be imposed on a previous porosity, as observed on other chondrites by Bland et al. (2006) and Consolmagno et al. (2008). The earlier porosity could be to degassing of sulfides during melting by impact event that may have contributed to develop the vesicles and holes. This latter process is supported by the presence of resorption features observed on enstatite crystals, holes on plagioclases and etch pits like bubbles on Cr-rich sulfides, which represent further proves of incompletely melting by shock events, as previously stated by Rubin (2016). On the other hand, excluding the precipitation of secondary phases that fill locally the voids (outer part of volume B2), the B1 and the inner part of B2 regions show a uniform pore distribution (Fig. 6). Actually, in the B1 and B2 regions open pores of 0.18–0.43 mm in size show the similar values of volume fraction (%) (Fig. 7). One possible explanation could be that part of voids were initially occupied by high-density phases, such as sulfides, homogeneously spread in the sample. The uniform distribution of these hypothetical primary phases and their successive disappearance that left the voids, would indicate a triggering phenomenon acting not only locally, but on the entire meteorite body such as an impact and/or high-grade metamorphism. These phases could be just sulfides and, as an example troilite, now almost not present. This hypothesis is in agreement with Lauretta et al. (1997), Rubin (2016) and Panerai et al. (2021). In particular, Panerai et al. (2021) found strong relationships between sulfide degassing and origin of porosity, analyzing by μ-CT two ordinary chondrites undergoing a range of temperatures from ambient to 1200C°.

On the contrary, distribution of closed pores is very different in the studied slab and shows lower concentration in volume B1 and higher value in the volume B2, particularly in its outer part (Fig. 6 and Fig. 7). This inhomogeneity can be related to the spatial distribution of the secondary high-density phases. The combined analyses on the B1 and B2 volumes of the slab, merging μ-CT data and SEM-EDS, allow us to associate the decrease of total porosity with the increase of the volume

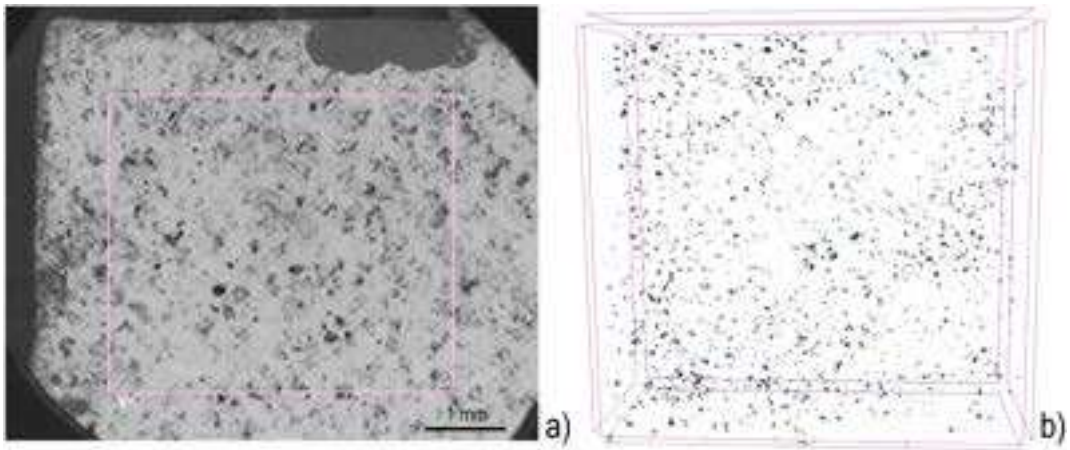

Fig. 8. B1 region of Al Haggounia 001 slab. a) SEM-BSE image; b) 3D volume rendering with phases corresponding to 100–255 of thresholds on grayscale histogram. Note the random distribution of the high-density phases.

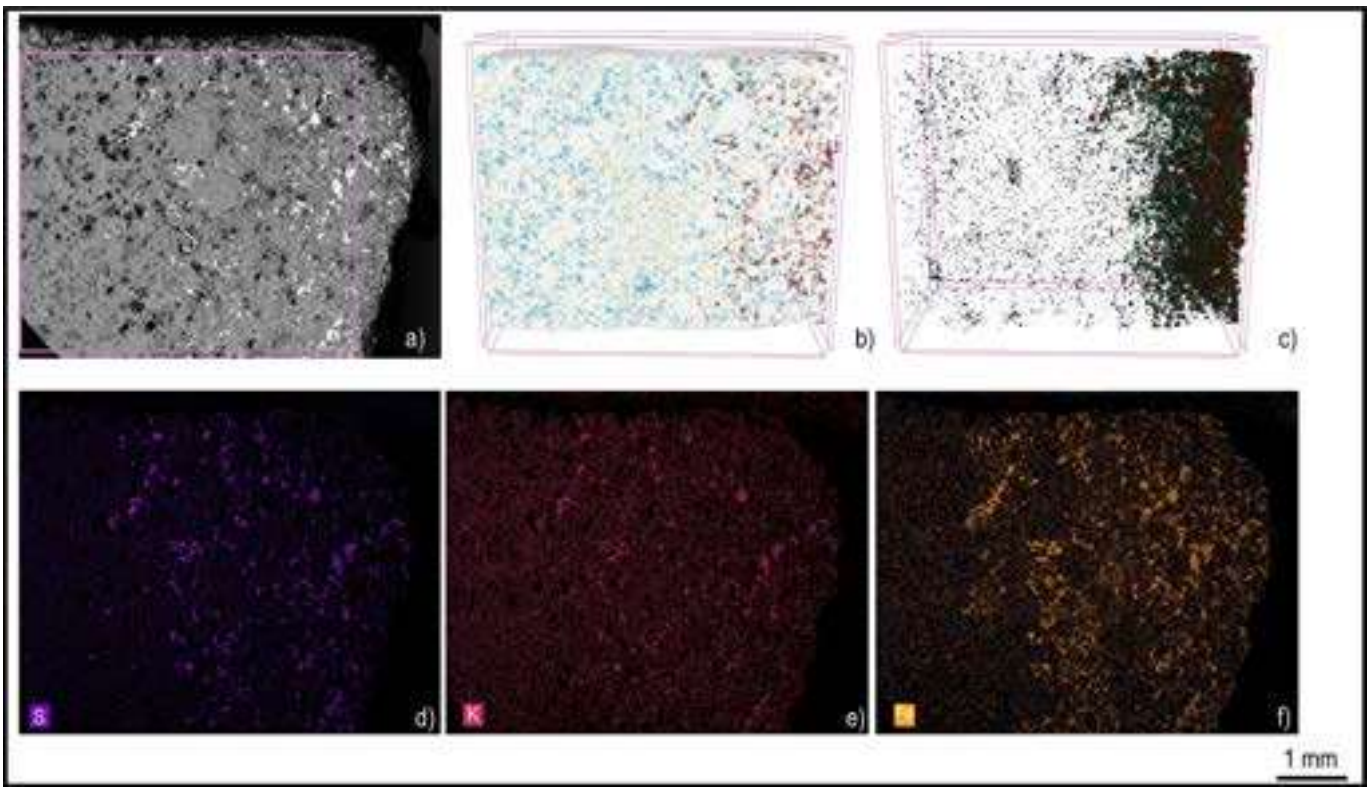

Fig. 9. B2 region of Al Haggounia 001 slab. a) SEM-BSE image; b) 3D volume rendering with phases corresponding to 100–255 of thresholds on grayscale histogram and open (blue) and closed pores (yellow); c) 3D volume rendering with only the high-density phases (100–255 of thresholds on grayscale histogram). d) SEM-EDS elemental map of S; e) SEM-EDS elemental map of K; SEM-EDS elemental map of Fe. Note the increase of high-density phases in the outer part, corresponding to the presence of Fe-rich phases and Jarosite (see K elemental map). (For interpretation of the references to colour in this figure legend, the reader is referred to the web version of this article.)

percentages of both the high-density phases and the closed pores in the outer part of the B2 region (Fig. 8 and Fig. 9), suggesting that secondary phases, such as jarosite, iron oxides and hydroxides, fill up in part the porosity, reducing it and favoring the formation of closed pores. This phenomenon seems to interest mainly the fragment region more exposed to terrestrial weathering, where a high concentration of jarosite was found (Fig. 9).

Our results, therefore, suggest that the high porosity found in Al Haggounia 001 fragment could be due to different events: an earlier porosity occurred during melting by impact event, the degassing and evaporating of sulfides left voids and vesicles and produced resorption features by partial melting also on silicates, preserving some relict chondrules. The secondary porosity occurred successively, after the fall of meteorite. A severe weathering affected this meteorite for a long time, producing the oxidation and partial dissolution of kamacite and the residual sulfides. This process developed preferentially along the porosity already present enlarging the previous pores and vesicles and in part filling up locally some of them by the precipitation of terrestrial phases derived by the oxidation of primary phases.

5. Conclusions

The volumetric data acquired on the internal structure and grain features of Al Haggounia 001 add new elements to this heterogeneous meteorite. A new estimation of total porosity for Al Haggounia 001, the differentiation between open and closed pores and the interpretation of the relationships between the spatial distribution of voids and the different mineralogical phases suggest different genetic processes of voids formation. The resorption features and the almost homogeneous distribution of open pores heavily support the previous hypothesis of Rubin (2016) who assigned the formation of voids and vesicles to degassing and evaporating of sulfides (mainly troilite) during melting by impact events. Conversely, the presence of closed pores can be ascribed to a severe terrestrial weathering, that enlarged the previous pores and locally modified the exposed pores, determining a partial filling by precipitation of secondary phases.

With this work we show the importance of a methodological approach that investigate a volume of a fragment of meteorite, providing a reconstruction of the spatial distribution of mineralogical phases and voids, their volume percentage, shape, and size. The volumetric analyses reduce the error generally related to data acquired on nearly bidimensional sample such as a thin section, minimizing the risk to obtain dissimilar information on different fragments of the same meteorite.

Declaration of Competing Interest

The authors declare that they have no known competing financial interests or personal relationships that could have appeared to influence the work reported in this paper.

Acknowledgements

The authors are very grateful to the Editor Prof. N. Malaspina, to the reviewer dr. Ioannis Baziotis, and to the anonymous reviewer for their constructive comments and suggestions that allowed appreciable improvement of the manuscript. The authors are grateful also to Nicola Mongelli for assistance during the SEM analyses.

Appendix A. Supplementary data

Supplementary data to this article can be found online at https://doi.

org/10.1016/j.lithos.2022.107015.

References

Agrosì, G., Tempesta, G., Mele, D., Caggiani, M.C., Mangone, A., Della, Ventura G., Cestelli-Guidi, M., Allegretta, I., Hutchison, M.T., Nimis, P., Nestola, F., 2019. Multiphase inclusions associated with residual carbonate in a transition zone diamond from Juina (Brazil). Lithos 350-351. https://doi.org/10.1016/j.lithos.2019.105279.

Alexayeve, K.N., 1958. Physical properties of stony meteorites and their interpretation based on the hypothesis on the origin of meteorites. Meteoritika 16, 67–77.

Alwmark, C., Schmitz, B., Holm, S., Marone, F., Stampanoni, M., 2011. A 3-D study of mineral inclusions in chromite from ordinary chondrites using synchrotron radiation X-ray tomographic microscopy—Method and applications. Meteorit. Planet. Sci. 46, 1071–1081. https://doi.org/10.1111/j.1945-5100.2011.01214.x.

Bam, L.C., Miller, J.A., Becker, M., 2020. A mineral X-ray linear attenuation coefficient tool (MXLAC) to assess mineralogical differentiation for X-ray computed tomography scanning. Minerals 10, 441. https://doi.org/10.3390/min10050441.

Bland, P.A., Zolensky, M.E., Benedix, G.K., Sephton, M.A., 2006. Weathering of chondritic meteorites. In: Chapter in Book: Meteorites and the Early Solar System II. University of Arizona Press, Publisher, pp. 853–867. https://doi.org/10.2307/j.ctv1v7zdmm.45.

Bunch, T., Wittke, J., Irving, A.J., 2014. http://www4.nau.edu/meteorite/Meteorite/Al_Haggounia.html.

Chennaoui-Aoudjehane, H., Jambon, A., Rjimati, E., 2007. Al Haggounia (Morocco) strewn field. Meteorit. Planet. Sci. 42, A30.

Consolmagno, G., Britt, D., Macke, R., 2008. The significance of meteorite density and porosity. Geochemistry 68 (1), 1–29. https://doi.org/10.1016/j.chemer.2008.01.003.

Dionnet, Z., Suttle, M.D., Longobardo, A., Rotundi, A., Folco, L., Della, Corte V., King, A., 2020. X-ray computed tomography: morphological and porosity characterization of giant Antarctic micrometeorites. Meteorit. Planet. Sci. 55, 1581–1599. https://doi.org/10.1111/maps.13533.

El Abassi, D., Ibhi, A., Faiz, B., Aboudaoud, I., 2013. A simple method for the determination of the porosity and tortuosity of meteorites with ultrasound. J. Geophys. Eng. 10 (5) https://doi.org/10.1088/1742-2132/10/5/055003.

El Goresy, A., Lin, Y., Miyahara, M., Gannoun, A., Boyet, M., Ohtani, E., Gillet, P., Trieloff, M., Simionovici, A., Feng, L., And, Lemelle L., 2017. Origin of EL3 chondrites: evidence for variable C/O ratios during their course of formation—a state of the art scrutiny. Meteorit. Planet. Sci. 52 (5), 781–806. https://doi.org/10.1111/maps.12832781. ©The Meteoritical Society, 2017.

Hanna, R.D., Ketcham, R.A., Hanna, Romy D., Ketcham, Richard A., 2017. X-ray computed tomography of planetary materials: A primer and review of recent studies. Geochemistry 77 (4), 547–572. ISSN 0009-2819. https://doi.org/10.1016/j.chemer.2017.01.006.

Feldkamp, L.A., Davis, L.C., Kress, J.W., 1984. Practical cone-beam algorithm. J. Optical Soc. Am. A-optics Image Sci. Vision 1, 612–619.

Hanna, R.D., Ketcham, R.A., Edey, D.R., O'Connell, J., 2022. 3D porosity structure of the earliest solar system material. Sci. Rep. 12, 8369. https://doi.org/10.1038/s41598-022-11976-1.

Hayes, J.H., Riebe, C.S., Holbrook, W.S., Flinchum, B.A., Hartsough, P.C., 2019. Porosity production in weathered rock: where volumetric strain dominates over chemical mass loss. Sci. Adv. 5 https://doi.org/10.1126/sciadv.aao0834.

Irving, A.J., Bunch, T.E., Rubin, A.E., Wasson, J.T., 2010. Northwest Africa 2828/Al Haggounia 001 Is a Weathered, Unequilibrated EL Chondrite: Trace Element and Petrologic Evidence, Meteoritics and Planetary Science Supplement, p. 73.

Jaques, V.A.J., Plessis, A.D., Zemek, M., Salplachta, J., Stubianova, Z., Zikmund, T., 2021. Review of porosity uncertainty estimation methods in computed tomography dataset. Meas. Sci. Technol. 32, 122001 https://doi.org/10.1088/1361-6501/ac1b40.

Kalasová, D., Zikmund, T., Spurný, P., Haloda, J., Borovička, J., Kaiser, J., 2020. Chemical and physical properties of Zd'ar nad Sazavou L chondrite and porosity differentiation using computed tomography. Meteorit. Planet. Sci. 9, 1073–1079. https://doi.org/10.1111/maps.13460.

Keil, K., 1962. Quantitativ-erzmikroskopische Integrationsanalyse der Chondrite. Chem. Erde 22, 281–348.

Krzesińska, A.M., Wirth, R., Kusiak, M.A., 2019. Petrogenesis of ungrouped enstatite meteorite Zakłodzie: fabric, texture, and nanostructure analysis for identification of mechanisms responsible for chondrite–achondrite transition. Meteorit. Planet. Sci. 54, 1462–1477. https://doi.org/10.1111/maps.13296.

Kuehner, S.M., Irving, A.J., Bunch, T.E., Wittke, J.H., 2006. EL3 Chondrite (not Aubrite) Northwest Africa 2828: An Unusual Paleo-meteorite Occurring as Cobbles in a Terrestrial Conglomerate (abstract #P51E-1247). American Geophysical Union, Fall Meeting 2006.

Lauretta, D.S., Lodders, K., Fegley, B., 1997. Experimental simulations of sulfide formation in the solar nebula. Science (New York, N.Y.) 277. https://doi.org/10.1126/Science.277.5324.358, 358–60. PMID 9219690.

Li, S.J., Wang, S.J., Miao, B.K., Li, Y., Li, X.Y., Zeng, X.J., Xia, Z.P., 2019. The density, porosity, and pore morphology of fall and find ordinary chondrites. J. Geophys. Res.: Planets 124, 2945–2969. https://doi.org/10.1029/2019JE005940.

Lowe, J.J., Hill, D.H., Domanik, K.J., Lauretta, D.S., Drake, M.J., Killgore, M., 2005. NWA 2736: an unusual new graphite-bearing aubrite. In: 36th Annual Lunar and Planetary Science Conference.

McCubbin, F.M., 2017. A low O/Si ratio on the surface of mercury: evidence for silicon smelting? J. Geophys. Res. (Planets) 122 (10), 2053–2076. https://doi.org/10.1002/2017JE005367.

McCubbin, F.M., Riner, M.A., Vander Kaaden, K.E., Burkemper, L.K., 2012. Is Mercury a volatile-rich planet? Geophys. Res. Lett. 39 (9) https://doi.org/10.1029/2012GL051711.

Nascimento-Dias, B.L., Araujo, O.M.O., Machado, A.S., Oliveira, D.F., Anjos, M.J., Lopes, R.T., Assis, J.T., 2019. Analysis of two meteorite fragments (lunar and martian) using X-Ray micro fluorescence and X-Ray computed microtomography techniques. Appl. Radiat. Isot. 152, 156–161. https://doi.org/10.1016/j.apradiso.2019.06.021. Epub 2019 Jun 19. PMID: 31302533.

Panerai, F., Bessire, B., Haskins, J., Foster, C., Barnard, H., Stern, E., Feldman, J., 2021. Morphological evolution of ordinary chondrite microstructure during heating: implications for atmospheric entry. Planet. Sci. J. 2 https://doi.org/10.3847/PSJ/ac1749.

Porfido, C., Manzari, P., Allegretta, I., Terzano, R., De Pascale, O., Senesi, G.S., 2020. Combined micro-X-ray fluorescence and micro computed tomography for the study of extraterrestrial volcanic rocks. The case of Northwest Africa (NWA) 8657: a shergottite martian meteorite. Talanta 217, 121114. https://doi.org/10.1016/j.talanta.2020.121114.

Pouchou, J.L., Pichoir, F., 1991. Quantitative analysis of homogeneous or stratified microvolumes applying the model "PAP". In: Heinrich, K.F.J., Newbury, D.E. (Eds.), Electron Probe Quantification. Plenum Press, New York, pp. 31–75. https://doi.org/10.1007/978-1-4899-2617-3_4.

Pratesi, G., Caporali, S., Loglio, F., Giuli, G., Dziková, L., Skála, R., 2014. Quantitative study of porosity and pore features in moldavites by means of X-ray micro-CT. Materials (Basel). https://doi.org/10.3390/ma7043319, 24;7(4):3319-3336. PMID: 28788620; PMCID: PMC5453340.

Rubin, A.E., 2015. Impact features of enstatite-rich meteorites. Geochemistry 75, 1–28. https://doi.org/10.1016/j.chemer.2014.09.001.

Rubin, A.E., 2016. Impact melting of the largest known enstatite meteorite: Al Haggounia 001, a fossil EL chondrite. k 51 (9), 1576–1587. https://doi.org/10.1111/maps.12679.

Soini, A.-J., Kukkonen, I.T., Kohout, T., Luttinen, A., 2020. Thermal and porosity properties of meteorites: a compilation of published data and new measurements. Meteorit. Planet. Sci. 55, 402–425. https://doi.org/10.1111/maps.13441.

Stacy, F.D., Lovering, J.F., Parry, L.G., 1961. Thermomagnetic properties, natural magnetic moments, and magnetic anisotropies of some chondritic meteorites. J. Geophys. Res. 66, 1523–1534. https://doi.org/10.1029/JZ066i005p01523.

Szurgot, M., Polanski, K., Kosinski, J.W., 2011. Microscopic studies of Al Haggounia 001 meteorite. In: Scientific Bulletin of the Technical University of Lodz, Physics, 32, pp. 65–74. https://doi.org/10.34658/physics.2011.32.65-74.

Tsuchiyama, A., Nakamura, T., Okazaki, T., Uesugi, K., Nakano, T., Sakamoto, K., Akaki, T., Iida, Y., Kadono, T., Jogo, K., Suzuki, Y., 2009. Three-dimensional structures and elemental distributions of Stardust impact tracks using synchrotron microtomography and X-ray fluorescence analysis. Meteorit. Planet. Sci. 44, 1203–1224. https://doi.org/10.1111/j.1945-5100.2009.tb01218.x.

Udry, A., Wilbur, Z.E., McCubbin, F.M., Vander Kaaden, K.E., Ziegler, K.G., De Felice, C., Mccoy, T., Gross, J., Turrin, B.D., 2019. Aubrite Meteorites as Geochemical Analogues to Mercury. https://ui.adsabs.harvard.edu/abs/2019AGUFM.P11B..01U.

Weisberg, M.K., Kimura, M., 2012. The unequilibrated enstatite chondrites. Geochemstry 72, 101–115. https://doi.org/10.1016/j.chemer.2012.04.003.

Zhang, M., Clark, B., King, A.J., Russell, S.S., Lin, Y., 2021. Shape and porosity of refractory inclusions in CV3 chondrites: a micro-computed tomography (μCT) study. Meteorit. Planet. Sci. 56, 500–514. https://doi.org/10.1111/maps.13635.

Zolotov, M.Y., Sprague, A.L., Hauck, S.A., Nittler, L.R., Solomon, S.C., Weider, S.Z., 2013. The redox state, FeO content, and origin of sulfur-rich magmas on Mercury. J. Geophys. Res. (Planets) 118, 138–146. https://doi.org/10.1029/2012JE004274.